Journal Pre-proof

Enhanced high-temperature strength of HfNbTaTiZrV refractory high-entropy alloy via Al$_2$O$_3$ reinforcement

Bingjie Wang , Qianqian Wang , Nan Lu , Xiubing Liang , Baolong Shen

Please cite this article as: Bingjie Wang , Qianqian Wang , Nan Lu , Xiubing Liang , Baolong Shen , Enhanced high-temperature strength of HfNbTaTiZrV refractory high-entropy alloy via Al$_2$O$_3$ reinforcement, *Journal of Materials Science & Technology* (2022), doi: https://doi.org/10.1016/j.jmst.2022.01.025

This is a PDF file of an article that has undergone enhancements after acceptance, such as the addition of a cover page and metadata, and formatting for readability, but it is not yet the definitive version of record. This version will undergo additional copyediting, typesetting and review before it is published in its final form, but we are providing this version to give early visibility of the article. Please note that, during the production process, errors may be discovered which could affect the content, and all legal disclaimers that apply to the journal pertain.

Article type: *Research article*

Enhanced high-temperature strength of HfNbTaTiZrV refractory high-entropy alloy via Al_2O_3 reinforcement

Bingjie Wang [a], Qianqian Wang [a,b], Nan Lu [c], Xiubing Liang [c,*], Baolong Shen [a,*]

[a] School of Materials Science and Engineering, Jiangsu Key Laboratory for Advanced Metallic Materials, Southeast University, Nanjing 211189, China

[b] School of Materials Science and Engineering, Jiangsu Key Laboratory of Advanced Structural Materials and Application Technology, Nanjing Institute of Technology, Nanjing 211167, China

[c] Defense Innovation Institute, Academy of Military Science, Beijing 100071, China

[*]Corresponding authors. E-mail addresses: liangxb_d@163.com (X.B. Liang); blshen@seu.edu.cn (B.L. Shen).

Highlights

- Oxide dispersion-reinforced HfNbTaTiZrV alloy with multiple strengthening mechanisms is fabricated by the addition of Al_2O_3 oxide.

- Nanoscale Al_2O_3 particles hinder the movement of dislocations and refine the grains from 80 to 13 μm.

- The interstitial strengthening improves the high temperature softening resistance of the studied alloy.

- 4vol.%Al_2O_3-reinforced alloy displays superior compressive yield strength of 1392 MPa at 800 °C and 693 MPa at 1000 °C.

- 4vol.%Al_2O_3 alloy displays notable characteristics of lightweight and high-temperature resistance.

Abstract

Novel composites of HfNbTaTiZrV refractory high-entropy alloy (RHEA) reinforced with 0-4 vol.% Al_2O_3 particles have been synthesized by vacuum arc melting. The microstructure evolution, compressive mechanical properties at room and elevated temperatures, as well as strengthening mechanism of the composites were analyzed. The HfNbTaTiZrV RHEA reinforced with 4 vol.% Al_2O_3 displayed excellent phase stability at elevated temperatures. A superior compressive yield strength of 2700 MPa at room temperature, 1392 MPa at 800 °C, and 693 MPa at 1000 °C was obtained for this composite. The improved yield strength resulted from multiple strengthening mechanisms caused by Al_2O_3 addition, including solution strengthening, interstitial strengthening, grain boundary strengthening, and dispersion strengthening. Besides, the effects of interstitial strengthening increased with temperature and was the main strengthening mechanism at elevated temperatures. These findings not only promote the development of oxide-reinforced RHEAs for challenging engineering applications but also provide guidelines for the design of light refractory materials with multiple strengthening mechanisms.

Keywords: Al_2O_3-reinforcement; HfNbTaTiZrV; Refractory high-entropy alloy; Interstitial strengthening.

1. Introduction

In the pursuit of high strength for metallic materials, high-entropy alloys (HEAs) with multiple principal elements have attracted extensive attention as a new class of metallic materials over the past two decades. The high configurational entropy of HEAs contributes to the decreased Gibbs free energy in these alloys, which retards the formation of intermetallics and stabilizes single solid solution phase [1-6]. Among them, refractory HEAs (RHEAs) that contain elements with high melting temperatures exhibit high strength at elevated temperatures and excellent radiation resistance in extreme environment, which are considered as promising materials for high-temperature applications such as shafts and turbines for aeroengines, wing tip leading edge of hypervelocity aircraft [7, 8]. Nevertheless, most RHEAs exhibit small ductility at room temperature and/or poor phase stability at high temperature. HfNbTaTiZr RHEA is one of the most thoroughly studied RHEAs with large ductility at room temperature and a small density of 9.9 g/cm^3, which makes it a potential substitution for Ni-based superalloy [9-11]. However, HfNbTaTiZr RHEA exhibits a low yield strength of 929 MPa at room temperature, which seriously limits its application. In addition, HfNbTaTiZr RHEA displays thermodynamic instability and phase decomposition at high temperatures. It was found the HfNbTaTiZr alloy annealed at 700 °C for only 2.5 h shows a phase decomposition of the originally body-centered-cubic (BCC) high entropy phase into a NbTa-rich BCC phase and ZrHf-rich hexagonal-close-packed (HCP) phases [12]. Therefore, it is crucial to improve the strength and phase stability of HfNbTaTiZr RHEA. Addition of metallic elements, oxides or oxygen atom has been reported to effectively improve the strength and hardness of HEAs. Firstly, alloying with V element can stabilize BCC phase and refine the grains, and thus leads to improvement of strength [13]. Senkov et al. reported that the addition of V improved the room-temperature yield strength of NbMoTaW RHEA from 1058 to 1246 MPa, and yield strength at 1600 °C was enhanced from 405 to 477 MPa [14]. They also

demonstrated that the solution of V in CrNbTiZr HEA nearly doubled the yield strength at 800 °C (from 115 to 259 MPa) [15]. Secondly, the addition of fine-scale oxide particles, including Y_2O_3, Al_2O_3, and TiO_2, to produce oxide dispersion strengthened (ODS) alloys is an effective means to improve the strength of alloys at room and elevated temperatures by reducing the grain size and inducing Orowan strengthening [16-18]. Because of the dispersion of Y_2O_3 particles, the grain size of ODS CoCrFeNiMn HEA reduced from 0.8 to 0.4 μm, while the yield strength increased from 1000 MPa to 1200 MPa [19]. Due to typical Orowan strengthening caused by Al_2O_3 particles, obvious improvement of the compressive yield strength is achieved in Al_2O_3-CoCrFeMnNi HEA, the yield strength increased from 1180 to 1600 MPa [20]. Thirdly, the addition of oxygen atoms in HEAs can overcome the strength-ductility trade-off through the interstitial strengthening. For example, due to the interstitial strengthening of oxygen atoms in HfNbZrTi HEA, the tensile yield strength increased from 776 to 1110 MPa. Besides, the elongation had nearly doubled, increasing from 14.3% to 27.7% [21].

However, the effect of the combination of above-mentioned three strengthening methods in ODS HEAs is rarely studied, and the contribution of each strengthening mechanism needs to be uncovered. In this work, we introduced V element and Al_2O_3 particles into HfNbTaTiZr RHEA by vacuum arc-melting. V element with high melting point is expected to stabilize phase structure and improve the strength of the alloy. Al_2O_3 was utilized as supplier for interstitial oxygen atoms to promote the interstitial strengthening and the oxide phases to introduce dispersion strengthening simultaneously. The effects of interstitial oxygen atoms and the nanoscale Al_2O_3 particles on the compressive mechanical properties of the HfNbTaTiZrV RHEA at room and elevated temperatures were investigated, the dominant strengthening mechanisms responsible for compressive properties were investigated.

2. Experimental

Al_2O_3-reinforced HfNbTaTiZrV ingots were prepared with pure metals (purity ＞99.99 wt%) and Al_2O_3 particles (purity＞99.9 wt%) by vacuum arc-melting in an argon atmosphere. x vol.% Al_2O_3-reinforced HfNbTaTiZrV (x = 0, 1, 2, 3, 4) RHEAs, hereinafter are referred to as HfNbTaTiZrV, 1 vol.% Al_2O_3, 2 vol.% Al_2O_3, 3 vol.% Al_2O_3, 4 vol.% Al_2O_3. Alloy ingots were remelted for more than 6 times to eliminate the composition segregation, and then drop-cast into a water-cooled copper mold with dimensions of Φ10 mm× 60 mm. The samples for compressive tests were cut into cylinders with 2 mm in diameter and 4 mm in height. The room-temperature compression tests were carried out at a crosshead strain rate of 1×10^{-3}/s using a Sans 5305 system, while the high-temperature compression tests were performed using a Zwick KAPPA 100 machine with the argon atmosphere. Crystal structure and phase constitution of the alloy was analyzed by X-ray diffractometer (XRD, Bruker D8-Discover) with Cu Kα radiation in a 2θ range from 20° to 100°. The atomic structure of samples was analyzed using a transmission electron microscope (TEM, Talos F200X). High angle annular dark field scanning (HAADF-STEM) images were recorded using an annular-type detector with collection semi-angle ~100-269 mrad. Volume fraction of the oxide phase was measured from TEM images by employing a commercial software package (Image-Pro-Plus) by using at least 6 TEM images from different grains. Elemental mappings of the samples were acquired by energy-dispersive spectroscopy (EDS). To prepare the samples for TEM analysis, thin foils were electro-polished to 3 mm in diameter and 50 μm in thickness by a DJ2000 twin-jet unit at around -35 °C by using a mixed solution of 6% perchloric acid, 30% *n*-butyl alcohol, and 64% methyl alcohol. Subsequently, the specimen was ion thinned by using a Gatan 691 iron beam thinner for around 30 min. The electron back-scattering diffraction (EBSD) images were obtained using a field emission scanning electron microscope (SEM, JSM-7800F). Specimens for EBSD analysis with dimensions of 10 × 10 × 1 mm^3 were electrochemically

polished by using a mixed solution of 6% perchloric acid, 30% *n*-butyl alcohol, and 64% methyl alcohol solution at a direct voltage of 30 V at room temperature.

3. Results

3.1. Phase identification

The XRD results of the as-cast *x* vol.% Al_2O_3 reinforced-HfNbTaTiZrV alloys are shown in Fig. 1. All diffraction peaks are indexed to the BCC crystalline structure. As shown in Fig. 1, the peak position of (110) diffraction tends to move towards lower value with the increasing amount of Al_2O_3, indicating that oxygen atoms exist as interstitials in the BCC crystalline lattice. Based on the Rietveld method [22], the lattice parameters of the 0-4 vol.% Al_2O_3 alloys are calculated to be 3.359 Å, 3.366 Å, 3.371 Å, 3.377 Å, and 3.381 Å, respectively. The presence of interstitial oxygen atoms increases the crystalline lattice parameter.

3.2. Mechanical properties

Fig. 2(a) shows the room-temperature compressive engineering stress-strain curves of the HfNbTaTiZrV alloys reinforced with 0-4 vol.% Al_2O_3 particles. The alloys exhibit work hardening in the compression process. The mechanical properties of the Al_2O_3-reinforced HfNbTaTiZrV alloys are listed in Table 1. The HfNbTaTiZrV alloy exhibits a yield strength of 1300 MPa. With the addition of 1 vol.%-4 vol.% Al_2O_3, the alloys exhibit a progressive increase in yield strength from 1986 to 2700 MPa. The HfNbTaTiZrV alloy displays 32% plastic strain and the addition of 1 vol.% Al_2O_3 do not cause significant reduction in the strain. However, a notable reduction in the plastic strain is observed in Al_2O_3-reinforced samples with content more than 2 vol.% of Al_2O_3. The oxide-reinforced HEAs exhibit higher strength at the expense of the plasticity of the alloy. This is typical mechanical behavior for ODS alloys [23, 24]. It is worth mentioning that although the plastic strain of 2 vol.%-4 vol.% Al_2O_3 alloys is small, it still shows work hardening in the

deformation process. The work hardening may come from the existence of the interstitial oxygen atom, which improves the critical shear stress necessary for dislocation nucleation and enables an excellent balance in interactions between dislocations and oxygen interstitials, thereby leads to a high strain-hardening reserve [21, 25, 26]. Thus, the alloys retain plastic deformation ability while the strength is improved.

Since the 4 vol.% Al_2O_3 alloy exhibits the highest yield strength at room temperature, it is chosen for elevated temperature compression. The compressive engineering stress-strain curves of the 4 vol.% Al_2O_3 alloy at 400, 600, 800, and 1000 °C are shown in Fig. 2(b). The strength of the alloy decreases with the increase of testing temperature. The work hardening phenomenon is kept during compression of the 4 vol.% Al_2O_3 alloy at 400 °C. At 600 °C and above, the alloy exhibits obvious dynamic recrystallization, which reaches the maximum strength at the initial stage of deformation, and strain softening occurs in the subsequent deformation [10]. 4 vol.% Al_2O_3 alloy shows excellent mechanical properties at high temperatures. The yield strength of 4 vol.% Al_2O_3 alloy is 1392 MPa at 800 °C and remains 693 MPa at 1000 °C.

3.3. Microstructure characterization

The fracture surfaces of the Al_2O_3-reinforced alloys after compressing at room temperature are shown in Fig. 3. With the increment of Al_2O_3 content, the fracture surface changes from ductile to quasi-cleavage fracture. As shown in Fig. 3(a), the HfNbTaTiZrV alloy shows a large number of dimples, which is typical ductile fracture morphology. Fig. 3(b) shows the fracture surface of the 1vol.%Al_2O_3 alloy. Compared with HfNbTaTiZrV alloy, the number of dimples decreases and quasi cleavage fracture morphology appears. The dimple morphology disappears and only quasi-cleavage fracture can be observed on the room-temperature fracture surfaces of the 2 vol.% Al_2O_3, and 4 vol.% Al_2O_3 alloys. As shown in Fig. 3(c, d), similar

8

fracture morphologies are observed in both alloys. The zigzag-shaped fracture surface indicates effective energy dissipation during deformation process, which ensures the alloy has a high strength and 6% plastic strain at the same time [16].

The grain structure of the as-cast HfNbTaTiZrV alloys reinforced with 0-4 vol.% Al_2O_3 particles characterized by EBSD analysis is displayed in Fig. 4. As shown in Fig. 4(a-e), the grains of Al_2O_3 reinforced-HfNbTaTiZrV alloy are refined with the increasing amount of Al_2O_3 apparently. It indicates that the changes in mechanical behavior are partly due to the addition of Al_2O_3 particles. The Al_2O_3 particles act as barrier for grain boundary migration, which significantly refine the grains. The grains of 4 vol.% Al_2O_3 alloys are smaller and more homogeneous (Fig. 4(e)). Fig. 4(f) shows the average grain size of the alloys. It reveals that the alloys consist of equiaxed grains with sizes varying in a wide range from 80 to 13 μm. Since the grain size of the oxide particle is small, both XRD and EBSD results of the alloys show single BCC phase. The oxide phase is characterized by TEM in Fig. 5.

The reason for the change of mechanical properties of the alloys is further uncovered from the TEM analyses. Bright-field TEM images of HfNbTaTiZrV and 1 vol.% Al_2O_3 alloys are shown in Fig. 5(a, b), respectively. The oxide particles can hardly be observed in the matrix of the 1 vol.% Al_2O_3 alloy, probably due to the low oxygen content. TEM images of 2 vol.% Al_2O_3 and 4 vol.% Al_2O_3 alloys are shown in Fig. 5(c, d), respectively. With the increasing content of oxygen atoms, brittle oxide phases gradually segregate in the alloy. Therefore, the strength increases with the increasing Al_2O_3 and the plastic strain decreases at the time.

Taking HfNbTaTiZrV and 4 vol.% Al_2O_3 alloys as examples, the distribution of oxygen atoms was investigated. HAADF-STEM mapping of the as-cast 4 vol.% Al_2O_3 alloy is shown in Fig. 6. Obvious element segregation can be observed in the 4 vol.% Al_2O_3 alloy and high content of oxygen atom is detected in the matrix. It indicates that oxygen atom changes the distribution of elements in the alloy matrix. Furthermore, it can be seen from Fig. 6 that some Al atoms are evenly distributed in

9

the matrix. Al atom with an atomic radius of 0.143 nm tends to form substitutional solid solution, which plays the role of solution strengthening and reduces the alloy density [27, 28].

Oxygen atom is observed all over the sample, further confirming it exists not only as oxides but also as interstitial solid solution atoms. This explains the phenomenon that the (110) diffraction peak shifts to the left from the XRD results in Fig. 1. To further identify the effects of Al_2O_3 addition on the microstructure evolution in the deformation process, bright-field TEM images of HfNbTaTiZrV and 4 vol.% Al_2O_3 alloys with 5% strain at room temperature are obtained. In Fig. 7(a), low-density dislocation entanglement can be observed in the HfNbTaTiZrV alloy, the dislocation motion is dominated by plane slip. The corresponding selected area electron diffraction (SAED) pattern is shown in Fig. 7(b), exhibiting BCC crystalline structure. Multiple ultrafine oxide particles are uniformly distributed in the matrix of 4 vol.% Al_2O_3 alloy, pinning and hindering the movement of dislocations during deformation. SAED pattern of the oxide phase in Fig. 7(c) (marked by green arrows) is shown in Fig. 7(d), which reveals that some of the nanoscale particles are Al_2O_3 viewed along the zone axis of $[001]_{Al2O3}$. The nanoscale Al_2O_3 particles contribute to dispersion strengthening, which is one of the reasons for the increase of yield strength.

Fig. 8(a, b) illustrates the high-resolution transmission electron microscopy (HRTEM) images of HfNbTaTiZrV and 4 vol.% Al_2O_3 alloys viewed along the [111] direction, respectively. The random distribution of the contrast indicates a random distribution of the constituent elements [29-31]. Inversed Fast Fourier Transform (FFT) images of the HfNbTaTiZrV and 4 vol.% Al_2O_3 alloys are shown in Fig. 8(c, d), respectively. The 4 vol.% Al_2O_3 alloy shows high density of lattice misfits, while no lattice misfit is observed in the HfNbTaTiZrV alloy. It confirms that the interstitial solution of oxygen atoms changes the lattice parameters and causes severe lattice distortion [26, 32]. To further verify this hypothesis, corresponding mappings

of the lattice strains along [121] were determined by using Peak Pairs Algorithm (PPA). As shown in Fig. 8(e, f), the 4 vol.% Al_2O_3 alloy has a less homogeneous distribution of lattice strains than the HfNbTaTiZrV alloy, revealing higher lattice distortion resulting from interstitials. Besides, as large lattice distortions impose more friction resistance to dislocation migration, the strength of 4 vol.% Al_2O_3 alloy is improved [26].

To evaluate the phase stability of the Al_2O_3-reinforced alloy at elevated temperatures, the XRD diffraction patterns of the alloy after 800 °C compression and annealing at 800 °C for 3 h are shown in Fig. 9(a). It can be seen that the alloys keep the same crystalline structure under two kinds of treatments at 800 °C as the as-cast 4 vol.% Al_2O_3 alloy. The corresponding bright-field TEM images and SAED pattern viewed along zone axis of $[110]_{BCC}$ are shown in Fig. 9(b, c), respectively. Based on the SAED patterns, the phase compositions of the alloys after compressing and annealing at 800 °C are the same as the those of as-cast 4 vol.% Al_2O_3 alloy. It mainly consists of BCC matrix and the Al_2O_3 particles. No phase decomposition is detected, which indicates that the 4 vol.% Al_2O_3 alloy exhibits excellent phase stability at 800 °C. EBSD image of the 4 vol.% Al_2O_3 alloy after 800 °C compression is shown in Fig. 9(d). The coarse grains are observed, which indicates that dynamic recrystallization fully completed at the deformation temperature. It proves that the decrease of yield strength at high temperatures is mainly due to the recrystallization softening [10]. Fig. 9(e) illustrates the polar figures of the 4 vol.% Al_2O_3 alloy compressed at various temperatures. The corresponding micro-textures also changed significantly. The maximum texture intensities of 4 vol.% Al_2O_3 alloy deformed at room temperature and 400 °C are 7.62 mud and 6.53 mud, respectively. When the alloy deformed above 600 °C, the preferred orientation of the alloy is evidently weakened by the dynamic recrystallization and the strength is reduced at the same time. This indicates texture strengthening induced by preferred orientation of grains during deformation contributes to the resistance to softening at elevated

temperatures. At present, the alloy still has the problem of room temperature brittleness. In the future research, the alloy can be further optimized by adjusting the texture volume fraction by controlling the growth of texture to expand the application of the alloy.

4. Discussion

4.1. Strengthening mechanisms

As revealed by the above analyses, it is inferred that the yield strength of 4 vol.% Al_2O_3 alloy is improved at room and elevated temperatures by the interstitial strengthening of oxygen atoms, the refined grains, the dispersion strengthening by Al_2O_3 particles simultaneously. The strengthening mechanisms of the Al_2O_3-reinforced HfNbTaTiZrV alloy at room and elevated temperatures can be summarized by four individual parts, including solution strengthening (σ_{ss}), interstitial strengthening (σ_{is}), grain boundary strengthening (σ_{gb}), and the dispersion strengthening (σ_{d}). The schematic diagram of the four strengthening mechanisms is shown in Fig. 10(a). In order to determine the contribution of each strengthening mechanism, the yield strength of the 4 vol.% Al_2O_3 alloy can be calculated as follows [33]:

$$\sigma_{0.2} = \Delta\sigma_{ss} + \Delta\sigma_{is} + \Delta\sigma_{gb} + \Delta\sigma_{d} \tag{1}$$

Take the calculation at room temperature as an example, σ_{ss} is the yield strength of the HfNbTaTiZrV alloy coming from solid solution at room temperature (983 MPa), and for 800 °C the value is 364 MPa. According to classical Hall-Petch relationship, the grain boundary strengthening (σ_{gb}) can be defined as [34]

$$\Delta\sigma_{gb} = \sigma_0 + k_y \frac{1}{d^{1/2}} \tag{2}$$

Here, σ_0 is the intrinsic frictional stress offered by the lattice, k_y is the Hall-Petch coefficient (390 MPa $\mu m^{1/2}$) [34], d is the average grain size. The strength increase caused by refined grain size can be derived as:

12

$$\Delta\sigma_{\mathrm{gb}} = k_{\mathrm{y}}(d_2^{-\frac{1}{2}} - d_1^{-\frac{1}{2}}) \tag{3}$$

In this study, d_1 is the average grain size for HfNbTaTiZrV alloy (80 μm), d_2 is the average grain size for 4 vol.% Al_2O_3 alloy (13 μm). Therefore, the strength increment caused by the grain boundary is calculated to be 82 MPa.

The increase in yield strength due to Al_2O_3 particles was estimated by using Ashby-Orowan relationship [35]:

$$\Delta\sigma_{\mathrm{p}} = M\frac{0.4Gb}{\pi\sqrt{1-v}} \cdot \frac{\ln(2\sqrt{\frac{2}{3}}r/b)}{2\sqrt{\frac{2}{3}}r(\sqrt{\frac{\pi}{4f_{\mathrm{v}}}}-1)} \tag{4}$$

Here, M is the Taylor factor, which is about 3.06 for BCC polycrystalline matrix, v=0.373 is the Poisson's ratio for HfNbTaTiV HEA and is used here as estimates [34]. G is the shear modulus. The Young' modulus of the base HEA is 128.09±7.6 GPa, obtained from compression measurements. The shear modulus is calculated by $G= E/2(1+ v)$, which is determined to be 56 GPa [21]. r =15 nm is the average radius of Al_2O_3 particles. f_{v} is the volume fraction of Al_2O_3 particles (2.6 vol.% for room temperature). b is the Burgers vector equals to $\sqrt{2}a/2$ (a is the lattice parameter, 3.381 Å). λ is the edge-to-edge distance between particles. Assuming spherical Al_2O_3 particles are distributed on a cubic grid, it can be calculated by the following equation [36]:

$$\lambda = 2\bar{\gamma}(\sqrt{\frac{\pi}{4f_{\mathrm{v}}}} - 1) \tag{5}$$

$\bar{\gamma} = \sqrt{2/3}\,\gamma$ is the mean radius of a circular cross in a random plane for a spherical oxide phase. Therefore, the increase in yield strength due to Al_2O_3 phase is calculated to be 356 MPa. Ultimately, the contribution from the interstitial strengthening (σ_{is}) is determined according to $\Delta\sigma_{\mathrm{is}} = \sigma_{0.2} - \sigma_{\mathrm{ss}} - \sigma_{\mathrm{gb}} - \sigma_{\mathrm{d}} = 1279$ MPa. The ratios of σ_{ss}, σ_{is}, σ_{gb}, σ_{d} are 36%, 47%, 3%, and 14%, respectively. Thus, the interstitial solution strengthening plays an important role in improving the strength of the 4 vol.% Al_2O_3 alloy.

13

The contribution of various strengthening mechanisms of the 4 vol.% Al_2O_3 alloy during 800 °C compression at yield strain was calculated by using the same method. Here, we list the detailed parameters for strengthening calculation at elevated temperatures in Table. 2. The ratios of σ_{ss}, σ_{is}, σ_{gb}, and σ_d for 800 °C compression are 27%, 64%, 2%, and 7%, respectively. The comparison of various strengthening mechanisms at room and elevated temperatures are shown in Fig. 10(b, c), respectively. The results reveal that the contribution of interstitial strengthening exhibits a gradual increase from 47% to 64% in the compressive yield strength when the experimental temperature increases from 25 to 800 °C, while the dispersion strengthening increases slightly. The reduction degree of each strengthening mechanism, which is defined as $\delta=(\sigma_{RT}-\sigma_{800°C})/\sigma_{RT}$, is totally different. δ_{ss}, δ_{is}, δ_{gb}, and δ_d are 64%, 29%, 52%, and 70%, respectively, suggesting the variation of the contribution from different strengthening mechanisms when the temperature changes. Based on the strengthening mechanism calculation, we can infer that interstitial strengthening improves the high-temperature softening resistance of the alloy.

4.2. Mechanical property comparison of RHEAs

Mechanical properties of 4 vol.% Al_2O_3 alloy at 400, 600, 800, 1000 and 1200 °C are compared with some recently reported RHEAs [7, 11, 14, 15, 37-42]. As shown in Fig. 11(a), the 4 vol.% Al_2O_3 alloy possesses a unique advantage at temperatures above 800 °C. At 800 °C, the yield strength of 4 vol.% Al_2O_3 alloy is almost three times higher than that of NbMoTaW of 552 MPa, and is higher by 65% than that of MoNbTaWV alloy of 846 MPa. Even at 1000 °C, it is higher by 26% than that of MoNbTaW of 548 MPa. In addition, comparisons of density and yield strength at 800 and 1000 °C are shown in Fig. 11(b). 4 vol.% Al_2O_3 alloy has a relatively lower density of 9.26 g/cm^3 and higher strength among the RHEAs. Compared with the high-density alloys such as MoNbTaW (13.61 g/cm^3) and

MoNbTaWV (12.29 g/cm^3), 4 vol.% Al_2O_3 alloy displays notable characteristics of lightweight and high-temperature resistance.

5. Conclusions

In summary, this work uncovers that proper addition of Al_2O_3 oxide in HfNbTaTiZrV RHEA strengthened the alloy at room and elevated temperatures. 4 vol.% Al_2O_3 alloy exhibited a strength of 2700 MPa at room temperature, 1392 MPa at 800 °C, and 693 MPa at 1000 °C. The addition of Al_2O_3 induced interstitial strengthening, grain boundary strengthening simultaneously, and dispersion strengthening. On one hand, the interstitial solution of oxygen atoms increased the lattice distortion and displayed excellent interstitial strengthening effect. On the other hand, the Al_2O_3 particles not only pinned at the grain boundary to inhibit the grain growth and refine the grain, but also hindered the movement of dislocation. Dynamic recrystallization was mainly responsible for the decrease of strength at elevated temperatures. Texture was developed and the alloy could be further optimized by adjusting the texture volume fraction. This work reveals the feasibility of adding oxide particles through vacuum arc-melting to improve the mechanical properties and phase stability of RHEAs at elevated temperatures, which broadens the application range of light refractory high entropy alloys.

Declaration of Competing Interest

The authors report no declarations of interest.

Acknowledgments

References

[1] J.W. Yeh, S.K. Chen, S.J. Lin, J.Y. Gan, T.S. Chin, T.T. Shun, C.H. Tsau, S.Y. Chang, Adv. Eng. Mater. 6 (2004) 299-303.

[2] B. Cantor, I.T.H. Chang, P. Knight, A.J.B. Vincent, Mater. Sci. Eng. A 375-377 (2004) 213-218.

[3] Z.D. Han, H.W. Luan, X. Liu, N. Chen, X.Y. Li, Y. Shao, K.F. Yao, Mater. Sci. Eng. A 712 (2018) 380-385.

[4] S.Y. Wu, D.X. Qiao , H.T. Zhang, J.W. Miao, H.L. Zhao, J. Wang, Y.P. Lu, T.M. Wang, T.J. Li, J. Mater. Sci. Technol. 97 (2022) 229-238.

[5] Q.J. Li, H. Sheng, E. Ma, Nat. Commun. 10 (2019) 3563.

[6] Y. Wu, F. Zhang, X.Y. Yuan, H.L. Huang, X.C. Wen, Y.H. Wang, M.Y. Zhang, H.H. Wu, X.J. Liu, H. Wang, S.H. Jiang, Z.P. Lu, J. Mater. Sci. Technol. 62 (2021) 214-220.

[7] D.B. Miracle, O.N. Senkov, Acta Mater. 122 (2017) 448-511.

[8] Q. Wang, J.C. Han, Y.F. Liu, Z.W. Zhang, C. Dong, Peter K. Liaw, Scr. Mater. 190 (2021) 40-45.

[9] B. Gwalani, S. Gorsse, D. Choudhuri, M. Styles, Y. Zheng, R.S. Mishra, R. Banerjee, Acta Mater. 153 (2018) 169-185.

[10] R.R. Eleti, A.H. Chokshi, A. Shibata, N. Tsuji, Acta Mater. 183 (2020) 64-77.

[11] O. Senkov, J. Scott, S. Senkova, F. Meisenkothen, D. Miracle, C. Woodward, J. Mater. Sci. 47 (2012) 4062-4074.

[12] S.Y. Chen, Y. Tong, K.K. Tseng, J.W. Yeh, J.D. Poplawsky, J.G. Wen, M.C. Gao, G. Kim, W. Chen, Y. Ren, R. Feng, W.D. Li, P.K. Liaw, Scr. Mater. 158 (2019) 50-56.

[13] M. Wang, Z. Ma, Z. Xu, X. Cheng, Scr. Mater. 191 (2021) 131-136.

[14] O.N. Senkov, G. Wilks, J. Scott, D.B. Miracle, Intermetallics 19 (2011) 698-706.

[15] O.N. Senkov, S.V. Senkova, C. Woodward, D.B. Miracle, Acta Mater. 61 (2013) 1545-1557.

[16] X. Duan, D. Jia, Z. Wu, Z. Tian, Z. Yang, S. Wang, Y. Zhou, Scr. Mater. 68 (2013) 104-107.

[17] M.Y. Li, Y.H. Guo, W.M. Li, Y.W. Zhang, Y.Q. Chang, Mater. Sci. Eng. A 817 (2021) 141368.

[18] X.C. Wen, Y. Wu, H.L. Huang, S.H. Jiang, H. Wang, XJ. Liu, Y. Zhang, X.Z. Wang, Z.P. Lu, Mater. Sci. Eng. A 805 (2021) 140798.

[19] B. Gwalani, R.M. Pohan, O.A. Waseemc, T. Alam, S.H. Hong, H.J. Ryu, R. Banerjee, Scr. Mater. 162 (2019) 477-481.

[20] Ł. Rogal, D. Kalita, L.L. Dobrzynska, Intermetallics 86 (2017) 104-109.

[21] Z.F. Lei, X.J. Liu, Y. Wu, H. Wang, S.H. Jiang, S.D. Wang, X.D. Hui, Y.D. Wu, B. Gault, P. Kontis, D. Raabe, L. Gu, H.W. Chen, H.T. Wang, J.B. Liu, K. An, Q.S. Zeng, T.G. Nieh, Z.P. Lu, Nature 563 (2018) 546-550.

[22] R.A. Young, The Rietveld Method, Oxford University Press, 1993.

[23] H. Hadraba, Z. Chlup, A. Dlouhy, Fe. Dobes, P. Roupcova, M. Vilemova, J. Matejicek, Mater. Sci. Eng. A 689 (2017) 252-256.

[24] M. Tane, T. Nakano, S. Kuramoto, M. Niinomi, N. Takesue, H. Nakajim, Acta Mater. 61 (2013) 139-150.

[25] Q.Q. Wei, L.Q. Wang, Y.F. Fu, J.N. Qin, W.J. Lu, D. Zhang, Mater. Des. 32 (2011) 2934-2939.

[26] Y.X. Ye, B. Ouyang, C.Z. Liu, G.J. Duscher, T.G. Nieh, Acta Mater. 199 (2020) 413-424.

[27] J.Y. He, W.H. Liu, H. Wang, Y. Wu, X.J. Liu, T.G. Nieh, Z.P. Lu, Acta Mater. 62 (2014) 105-113.

[28] S.F. Ge, H.M. Fu, L. Zhang, H.H. Mao, H. Li, A.M. Wang, W.R. Li, H.F. Zhang, Mater. Sci. Eng. A 784 (2020) 139275.

[29] Y. Chen, Y. Li, X. Cheng, Z. Xu, C. Wu, B. Cheng, M. Wang, Mater. Lett. 228 (2018) 145-147.

[30] J.A. Smeltzer, B.C. Hornbuckle, A.K. Giri, K.A. Darling, M.P. Harmer, H.M.

Chan, C.J. Marvel, Acta Mater. 211 (2021) 116884.

[31] Y.X. Ye, B. Ouyang, C.Z. Liu, G.J. Duscher, T.G. Nieh, Acta Mater. 199 (2020) 413-424.

[32] Y. Liu, G.P. Zheng, M Li, J. Alloys Compd. 843 (2020) 15606.

[33] F. He, D. Chen, B. Han, Q. Wu, Z. Wang, S. Wei, D. Wei, J. Wang, C. Liu, J.J. Kai, Acta Mater. 167 (2019) 275-286.

[34] Z.B. An, S.C. Mao, Y.N. Liu, L. Wang, H. Zhou, B. Gan, Z. Zhang, X.D. Han, J. Mater. Sci. Technol. 79 (2021) 109-117.

[35] T. Xiong, S.J. Zheng, J.Y. Pang, X.L. Ma, Scr. Mater. 186 (2020) 336-340.

[36] I. Moravcik, H. Hadraba, L.L. Li, I. Dlouhy, D. Raabe, Z.M. Li, Scr. Mater. 178 (2020) 391-397.

[37] Z.D. Han, N. Chen, S.F. Zhao, L.W. Fan, G.N. Yang, Y. Shao, K.F. Yao, Intermetallics 84 (2017) 153-157.

[38] N.N. Guo, L. Wang, L.S. Luo, X.Z. Li, Y.Q. Su, J.J. Guo, H.Z. Fu, Mater. Des. 81 (2015) 87-94.

[39] C.C. Juan, M.H. Tsai, C.W. Tsai, C.M. Lin, W.R. Wang, C.C. Yang, S.K. Chen, S.J. Lin, J.W. Yeh, Intermetallics 62 (2015) 76-83.

[40] O.N. Senkov, S. Gorsse, D.B. Miracle, Acta Mater. 175 (2019) 394-405.

[41] Y. Zhang, Y. Liu, Y. Li, X. Chen, H. Zhang, Mater. Lett. 174 (2016) 82-85.

[42] O.N. Senkov, D.B. Miracle, K.J. Chaput, J.P. Couzinie, J. Mater. Res. 33 (2018) 3092-3128.

Figures and Tables

Table. 1 Compressive mechanical properties for *x* vol.% Al_2O_3-reinforced HfNbTaTiZrV alloys at room temperature.

Table. 2 Parameters for strengthening mechanism calculation for HfNbTaTiZrV and 4 vol.% Al_2O_3 alloys during 800 ° C compression at yield strain.

Fig. 1. XRD patterns of the as-cast *x* vol.% Al_2O_3-reinforced HfNbTaTiZrV alloys at room temperature.

Fig. 2. Compressive engineering stress-strain curves of (a) the as-cast 0-4 vol.% Al_2O_3-reinforced HfNbTaTiZrV alloys at room temperature, (b) 4 vol.% Al_2O_3 alloy at elevated temperatures.

Fig. 3. Fracture surfaces of the Al_2O_3-reinforced alloys compressed at room temperature (a) HfNbTaTiZrV alloy, (b) 1 vol.% Al_2O_3 alloy, (c) 2 vol.% Al_2O_3 alloy, (d) 4 vol.% Al_2O_3 alloy.

Fig. 4. EBSD images of the as-cast Al_2O_3-reinforced HfNbTaTiZrV alloys at room temperature (a) HfNbTaTiZrV alloy, (b) 1 vol.% Al_2O_3 alloy, (c) 2 vol.% Al_2O_3 alloy, (d) 3 vol.% Al_2O_3 alloy, (e) 4 vol.% Al_2O_3 alloy, (f) Average grain size of the alloys.

Fig. 5. Bright-field TEM images as-cast Al_2O_3-reinforced alloys (a) HfNbTaTiZrV alloy, (b) 1 vol.% Al_2O_3 alloy, (c) 2 vol.% Al_2O_3 alloy, (d) 4 vol.% Al_2O_3 alloy.

Fig. 6. HAADF-STEM micrograph of the as-cast 4 vol.% Al_2O_3 alloy along the [110] zone axis (Im-3m) and EDS mappings showing the distribution of elements.

Fig. 7. Bright-field TEM images of alloy with 5% strain at room temperature (a) HfNbTaTiZrV alloy, (b) SAED pattern of (a), (c) 4 vol.% Al_2O_3 alloy, (d) SAED pattern of (c).

Fig. 8. Lattice uniformity analysis of the HfNbTaTiZrV and 4 vol.% Al_2O_3 alloy alloys (a) and (b) HRTEM images of the HfNbTaTiV and 4 vol.% Al_2O_3 alloys viewed in [110] direction, respectively. (c) and (d) Inversed FFT images of (a) and (b), respectively. (e) and (f) Distribution maps of interatomic distances along [121]

in the HfNbTaTiZrV and 4 vol.% Al_2O_3 alloys, respectively.

Fig. 9. Microstructure of the 4 vol.% Al_2O_3 alloy (a) X-ray diffraction patterns of various treatment, (b) Bright-field TEM image of the 4 vol.% Al_2O_3 alloy after 800 °C compression, (c) Bright-field TEM image of the 4 vol.% Al_2O_3 alloy after annealing at 800 °C for 3 h, (d) EBSD image of the 4 vol.% Al_2O_3 alloy after 800 °C compression, (e) Pole figures for $\{110\}_{BCC}$ of the 4 vol.% Al_2O_3 alloy deformed at various temperatures.

Fig. 10. (a) Schematic diagram of the solid strengthening, interstitial strengthening, grain boundary strengthening, and dispersion strengthening, respectively. Contributions of different strengthening mechanisms in the 4 vol.% Al_2O_3 alloy during compression at (b) Room temperature and (c) 800 °C.

Fig. 11. Mechanical property comparison between the 4 vol.% Al_2O_3 alloy and other RHEAs (a) Temperature dependence on the yield strength, (b) Density-yield strength at elevated temperatures of 800 and 1000 °C.

Properties	Alloys					
	HfNbTaTiZrV	1vol.%Al_2O_3	2vol.%Al_2O_3	3vol.%Al_2O_3	4vol.%Al_2O_3	5vol.%Al_2O_3
Yield strength (MPa)	1300	1986	2149	2283	2700	2696
Fracture strength (MPa)	2246	3164	2467	2719	2739	2726
Plastic strain (%)	32	22	7	6.5	6	4

Table. 1

21

Alloy	Grain size d (μm)	Oxides radius r (nm)	Oxides fraction f_v (%)
HfNbTaTiZrV	203	—	—
4vol.%Al$_2$O$_3$	50	40	1.9

Table. 2
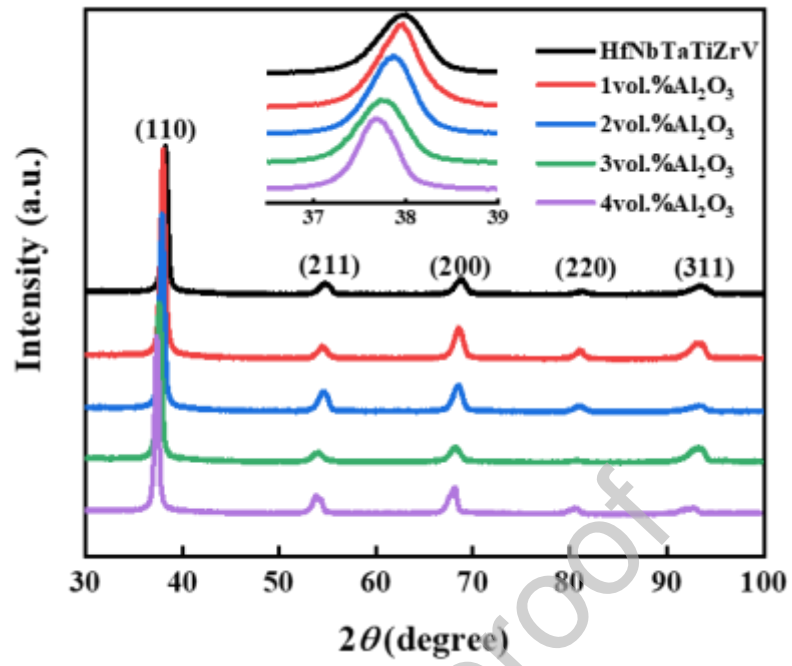
Fig. 1.

Fig. 2.

Fig. 3.

Fig. 4.

Fig. 5.

Fig. 6.

28

Fig. 7.

Fig. 8.

Fig. **9.**

31

Fig. 10.

Fig. 11.